Biomaterials 280 (2022) 121277

Contents lists available at ScienceDirect

Biomaterials

journal homepage: www.elsevier.com/locate/biomaterials

Intravital imaging and single cell transcriptomic analysis for engraftment of mesenchymal stem cells in an animal model of interstitial cystitis/bladder pain syndrome

Hwan Yeul Yu [a,b,h,1], Seungun Lee [b,c,1], Hyein Ju [b,c], Youngkyu Kim [d,e], Jung-Hyun Shin [a], HongDuck Yun [b,c], Chae-Min Ryu [a,b], Jinbeom Heo [b,c], Jisun Lim [b,c], Sujin Song [b,c], Sanghwa Lee [d,e], Ki-Sung Hong [f,g], Hyung-Min Chung [f,g], Jun Ki Kim [d,e], Myung-Soo Choo [a,**], Dong-Myung Shin [b,c,*]

[a] Department of Urology, Asan Medical Center, University of Ulsan College of Medicine, Seoul, South Korea
[b] Department of Biomedical Sciences, Asan Medical Center, University of Ulsan College of Medicine, Seoul, South Korea
[c] Department of Physiology, Asan Medical Center, University of Ulsan College of Medicine, Seoul, South Korea
[d] Biomedical Engineering Research Center, Asan Institute for Life Sciences, Asan Medical Center, Seoul, South Korea
[e] Department of Convergence Medicine, University of Ulsan, College of Medicine, Seoul, South Korea
[f] Department of Stem Cell Biology, School of Medicine, Konkuk University, Seoul, South Korea
[g] Mirae Cell Bio Co., Ltd., Seoul, South Korea
[h] ToolGen Inc., Seoul, South Korea

ARTICLE INFO

Keywords:
Intravital imaging
Single cell analysis
Mesenchymal stem cell
FOS
Interstitial cystitis/bladder pain syndrome

ABSTRACT

Mesenchymal stem cell (MSC) therapy is a promising treatment for various intractable disorders including interstitial cystitis/bladder pain syndrome (IC/BPS). However, an analysis of fundamental characteristics driving *in vivo* behaviors of transplanted cells has not been performed, causing debates about rational use and efficacy of MSC therapy. Here, we implemented two-photon intravital imaging and single cell transcriptome analysis to evaluate the *in vivo* behaviors of engrafted multipotent MSCs (M-MSCs) derived from human embryonic stem cells (hESCs) in an acute IC/BPS animal model. Two-photon imaging analysis was performed to visualize the dynamic association between engrafted M-MSCs and bladder vasculature within live animals until 28 days after transplantation, demonstrating the progressive integration of transplanted M-MSCs into a perivascular-like structure. Single cell transcriptome analysis was performed in highly purified engrafted cells after a dual MACS−FACS sorting procedure and revealed expression changes in various pathways relating to pericyte cell adhesion and cellular stress. Particularly, *FOS* and cyclin dependent kinase-1 (*CDK1*) played a key role in modulating the migration, engraftment, and anti-inflammatory functions of M-MSCs, which determined their *in vivo* therapeutic potency. Collectively, this approach provides an overview of engrafted M-MSC behavior *in vivo*, which will advance our understanding of MSC therapeutic applications, efficacy, and safety.

1. Introduction

Mesenchymal stem cells (MSCs) can repair tissue injury because they can engraft and regenerate tissue-specific cells after *in vivo* administration. In addition, these progenitor cells provide favorable microenvironments (including immune-modulatory, anti-inflammatory, and pro-angiogenic environments) by supplying growth factors, matrix proteins, and extracellular vesicles, and by mediating cell–cell interactions [1–3]. Multipotent MSCs can be isolated from several adult or fetal tissue types, such as bone marrow (BM), umbilical cord blood, and

* Corresponding author. Department of Biomedical Sciences, Asan Medical Center, University of Ulsan College of Medicine, 88 Olympic-ro 43-gil, Songpa-gu, Seoul, 05505, South Korea.
** Corresponding author. Department of Urology, Asan Medical Center, University of Ulsan College of Medicine, 88 Olympic-ro 43-gil, Songpa-gu, Seoul, 05505, South Korea.
E-mail addresses: mschoo@amc.seoul.kr (M.-S. Choo), d0shin03@amc.seoul.kr (D.-M. Shin).
[1] These authors contributed equally to this work.

https://doi.org/10.1016/j.biomaterials.2021.121277
Received 9 March 2021; Received in revised form 8 November 2021; Accepted 23 November 2021
Available online 27 November 2021
0142-9612/© 2021 Published by Elsevier Ltd.

amniotic fluid. MSCs were recently reported to be derived directly from pluripotent stem cells (PSCs) such as embryonic stem cells (ESCs) [4,5] and induced PSCs (iPSCs) [6,7]. This represents an attractive alternative for obtaining sufficient numbers of cells without the associated loss of function and heterogeneity resulting from *ex vivo* expansion of adult MSCs.

Because of these advantages, MSC-based therapies have been proposed to treat various intractable cardiovascular, musculoskeletal, neurological, immunological, and urological disorders [8,9]. However, their inconsistent outcomes have impeded their clinical applications [3]. More importantly, a lack of information regarding the fundamental characteristics of transplanted cell behavior *in vivo* has hindered the translation of promising preclinical studies into clinical practice. It has been suggested that dynamic monitoring of the biological and molecular properties of engrafted MSCs in pathological environments would not only facilitate this translation, but also enable the early prediction of the therapeutic effects of MSCs.

Recent advances in single cell analysis and live bio-imaging methods have paved the way for cellular and molecular mapping and high-resolution visualization of living cells or animals, respectively. For example, microfluidic single cell analysis of transplanted human iPSC-derived cardiomyocytes revealed that they release significant levels of pro-angiogenic and pro-survival factors in an acute myocardial infarction animal model [10]. Several intravital imaging platforms, including fluorescence microscopy [11,12], photoacoustic imaging [13,14], and multimodality imaging with positron emission tomography, computed tomography, and bioluminescence [15,16], have been used to study the dynamics of various cellular processes *in vivo*, such as stem cell trafficking and engraftment, intercellular interactions, and vascular changes. Intravital microscopy (IVM) techniques overcome the limitations of commonly used methods for mechanistic analysis, such as immunohistochemistry, which can only provide static insights at discrete time-intervals in different animals [11,17,18]. By providing both spatial and temporal information at single cell resolution, the dynamic interplay between engrafted cells and host micro-environments can be properly examined.

Previously, we employed a combination of intravital confocal fluorescence imaging and microcystoscopy in living animals to longitudinally monitor the distribution and phenotypic properties of transplanted multipotent-MSCs (M-MSCs) derived from human ESCs (hESCs) in two animal models of interstitial cystitis/bladder pain syndrome (IC/BPS) representing acute or chronic pathogenesis [19,20]. Importantly, the hESC-derived M-MSCs had improved *in vivo* engraftment without adverse outcomes when transplanted into two IC/BPS animal models, elucidating their superior therapeutic efficacy to their BM-derived counterparts [19–21]. However, in-depth information of the MSC engraftment process, particularly their interaction with the micro-environment and molecular profiles at the genome-wide level, remains to be determined.

In the present study, two-photon IVM imaging analysis provides evidence for the dynamic association between the engrafted M-MSCs and bladder vasculature in live animals, suggesting that the transplanted M-MSCs gradually integrated into a perivascular-like structure. Furthermore, the single cell transcriptomic profile of the engrafted cells in the pathological IC/BPS bladder included the expression of Fos proto-oncogene (FOS; AP-1 transcription factor subunit) and cyclin dependent kinase-1 (CDK1). These genes were crucial for modulating the migration, homing, function, and *in vivo* engraftment of the transplanted M-MSCs, and determined their therapeutic potency.

2. Materials and methods

2.1. Study approval

All animal experiments were approved by the Institutional Animal Care and Use Committee of the University of Ulsan College of Medicine (IACUC-2019-12-128 and IACUC-2017-12-054).

2.2. Culture of hESC-derived M-MSCs

M-MSCs differentiated from H9 hESCs [4] were maintained in EGM2-MV medium (Lonza, San Diego, CA, USA) on plates coated with rat tail collagen type I (Sigma-Aldrich, St. Louis, MO, USA) in a humidified atmosphere containing 5% CO_2 at 37 °C, as previously described [19,20]. M-MSCs at less than ten passages were used for *in vitro* cell culture and *in vivo* animal experiments. For ectopic expression of green fluorescent protein (GFP) or shRNA specific to *FOS* or *CDK1*, M-MSCs wereinfected with lentiviruses harboring the indicated constructs, as previously described [22]. The *in vitro* cellular and *in vivo* therapeutic functions were evaluated 4 days after lentiviral infection. Information about all reagents, resources, and the sequences of oligonucleotides in each shRNA used in this study are indicated in Table S1.

2.3. Animal models and administration of M-MSCs

Acute IC/BPS was induced in rats by HCl instillation, as previously reported [19,23]. In brief, 0.2 M HCl was instilled into 10-week-old female Sprague-Dawley rats (Orient Bio, Gapyeong, Korea). One week later, 1×10^6 M-MSCs or PBS vehicle were directly injected into the outer layer of the anterior wall and dome of the bladder. One week after M-MSC administration, the bladder voiding function and tissue damage were examined by unanesthetized and unrestrained cystometrogram (awake cystometry) and histological staining, respectively, according to our previous reports [19,20]. Therapeutic evaluations were performed in two independent sets of five animals per group, and histology was assessed in two randomly selected representative areas per slide in ten animals. Quantitative digital image analysis was performed using Image Pro 5.0 software (Media-Cybernetics, Rockville, MD, USA). The animals used in this study were randomly allocated to treatment groups, the order of HCl instillation, cell transplantation or vehicle injection, and cystometry. Investigators involved in surgical procedures were masked to information on the type of injected cells. All cystometric, histological, and gene expression assessments were performed by investigators who were blinded to treatment groups. Any animals that died unexpectedly by bladder insults or catheter implantation were excluded from any analyses.

For bio-imaging assays, HCl-IC/BPS was induced in 10-week-old female BALB/c-nu (CAnN.Cg-*Foxn1*^{nu}/CrlCrlj) immune-compromised mice (Charles River Laboratories, Yokohama, Japan). Subsequently, 1×10^5 M-MSCs stably expressing GFP or Nano-lantern construct [24] were administered for two-photon microscopic or IVIS bioluminescence imaging analysis, respectively. The M-MSCs were injected directly into the bladder serosa, as described in the rat animal model. The bioluminescence resonance energy transfer imaging was performed using IVIS Spectrum Preclinical *In vivo* Imaging System and Living Imaging 4.4 software (PerkinElmer, Waltham, MA, USA), according to the manufacturer's instructions and a previously published protocol [19,24].

2.4. Two-photon IVM imaging

Two-photon IVM was performed in five independent mic 3–28 days after transplantation. Mice were anasthetized by intraperitoneal injection of 30 mg/kg Zoletil (Virbac Laboratories, Carros, France) and secured on an externally heated imaging plate in a supine position. Blood vessels in each mouse were labeled by orbital injection of 100 μL Texas red-conjugated Dextran (70,000 MW; Sigma-Aldrich) at 1 mg/mL [25]. The bladder was exposed by a 3 mm incision in the abdomen and immobilized by mounting between a glass coverslip and an organ plate, manufactured in house by 3D-printing with poly lactic acid. GFP^+ engrafted cells and vascular luminal walls labeled with Texas red were visualized using a two-photon IVM (IVM-MS; IVIM Technology, Daejeon, Korea).

An ultrafast femtosecond pulse laser at 920 nm (Alcor 920; Spark Lasers, Martillac, France) was used as a two-photon excitation source. Fluorescence signals of GFP and Texas red were detected at 502.5–537.5 nm and 569.5–604.5 nm, respectively. Intravital images were obtained using a high numerical aperture water-immersion objective lens (CFI75 Apochromat 25XW, NA1.1; Nikon, Tokyo, Japan) with a field of view of 454 × 454 μm^2. The microscope was initially aligned near the M-MSC injection site, and the video-rate imaging was recorded. When locations with GFP$^+$ engrafted cells and blood flow were found, z-image stacks were acquired in 1–5 μm z-step intervals, with an average total depth of 223.4 μm (114–334 μm) from the outer layers of the bladder. As a negative control, little GFP signal was observed in the bladders before and up to 28 days after transplantation (DAT) of non-GFP expressing M-MSCs (data not shown).

2.5. Image processing and analysis

Image processing and analysis were performed using the commercial software program IMARIS 9.5 (Bitplane AG, Zurich, Switzerland). Using the surface function, z-stack images were 3-dimensionally reconstructed for volumetric analysis. Using the statistics function, the volumetric areas of GFP$^+$ cells and vascular luminal walls were calculated with identical thresholds of fluorescence intensity. The sphericity of cells was calculated using the following equation (where V_p is the volume of the cells, and A_p is the surface of the cells):

$$\psi = \frac{\pi^{\frac{1}{3}}(6V_p)^{\frac{2}{3}}}{A_P}$$

Using the distance transformation function, the distances between each GFP$^+$ cell and vessel were determined by measuring the shortest distance between the outer boundary of a GFP$^+$ cell, as volumetrically reconstructed surface, and the inner luminal wall of the vessel. Based on an approximate endothelial surface layer thickness of 1 μm, cells located <1 μm from a vessel wall were considered as being in contact with the vessel.

2.6. Labeling of magnetic nanoparticle resovist on M-MSCs

M-MSCs stably expressing GFP were seeded at a density of 2 × 10^6 cells, 2 h before Resovist labeling. Cells were labeled by incubation for 10 min with culture medium containing 500 μg/mL Ferucarbotran (Resovist; Bayer Schering Pharma, Berlin, Germany) and 5 μg/mL protamine sulfate (P3369, Sigma-Aldrich). The labeling medium was removed, and the cells were further cultivated for 24 h before *in vivo* administration.

2.7. Two consecutive MACS−FACS purifications of the engrafted M-MSCs

Bladders were isolated from three IC/BPS rats at the indicated DAT and minced into small pieces, andincubated with 2 mL Accutase (A1110501; Gibco, Waltham, MA, USA) at room temperature for 10 min. Erythrocytes were removed by RBC Lysis Solution (158,902; QIAGEN, Hilden, Germany). Single cell suspensions of bladder tissue were centrifuged at 6000×*g* for 20 min at 4 °C and resuspended in 1 mL magnetic activated cell sorting (MACS) buffer (low glucose DMEM containing 2.5% FBS and 1% HEPES). MACS sorting was performed by standing the resuspended cells in the magnetic device (12321D; Invitrogen, Waltham, MA, USA) at room temperature for 3 min, followed by two washes with MACS buffer to remove unbound cells. The Resovist$^+$ cells were further purified based on the expression of GFP by live fluorescence activated cell sorting (FACS) using an ARIAIII Flow Cytometer System (BD Biosciences, San Jose, CA, USA), as previously described [2,26]. To determine contamination by host cells, the levels of expression of rat β2 microglobin (B2MG) and human *GAPDH* mRNAs in the purified cell samples were quantified by real-time quantitative PCR (RQ-PCR) after each sorting procedure.

2.8. Single cell transcriptome analysis

Single cell cDNA libraries were synthesized as previously described [27]. Using an ARIAIII Flow Cytometer System, the Resovist$^+$/GFP$^+$ bladder cells (sorted by MACS−FACS) or trypsinized cultured M-MSC cells (control) were distributed as single cell into each well of a 96-well plate (Thermo Scientific, Waltham, MA, USA) containing 4.5 μL lysis buffer per well. RNA from each well was amplified into T7-primed single cell cDNA libraries as previously described [28]. Resovist$^+$/GFP$^+$ single cell cDNA libraries were initially screened by determining the expression of the host-originated rat *B2mg*, or genes relating to stem cell function, using the amplified T7-primed PCR products that were diluted 20-fold. Only single cell cDNA libraries with minimal host cell contamination were selected for the genome-wide analysis. The gel-eluted T7-primed libraries were biotin-labeled using the GeneChip® 3' *in vitro* transcription kit (Affymetrix, Santa Clara, CA, USA), starting from the protocol step "*In vitro Transcription to Synthesize Labeled aRNA.*"

Biotin-labeled aRNA from single cell libraries was fragmented and hybridized to the Affymetrix GeneChip® Human Genome U133 Plus 2.0 Array. Microarray image data were processed on GeneChip GCS3000 Scanner and Command Console software (Affymetrix). Raw data were extracted automatically by the Affymetrix data extraction protocol provided by Affymetrix GeneChip® Command Console® (AGCC) software.

Functional analysis of transcriptomes and core analyses of gene networks, biofunctions, and canonical pathways were performed using MetaCore (Clarivate Analytics, Philadelphia, PA, USA) or geneset enrichment analysis (GSEA) (Broad Institute, Cambridge, MA, USA) microarray software using default settings. For the MetaCore analyses, the cut-off values for genes were 1.5-fold up- or down-regulation and $p < 0.05$ significance. For GSEA, genesets were chosen from previous studies or filtered from a curated functional geneset (C2) database. Details of the significant genes and their biological processes and pathways from the MetaCore analysis, as well as genesets analyzed by GSEA, are described in Datasets S1 and S2, respectively.

2.9. In vitro molecular and cellular characterization of M-MSCs

The levels of mRNA and protein encoded by the selected genes were validated and quantified by RQ-PCR and western blotting, respectively, as previously described [22,29]. The levels of the indicated proteins were assessed by probing with monoclonal antibodies specific to FOS (#4384, Cell Signaling Technology, Danvers, MA, USA) and CDK1 (sc-54; Santa Cruz Biotechnology, Dallas, TX, USA), and normalized relative to the levels of β-ACTIN (A5441, Sigma-Aldrich) in the same samples. Primer sequences used for gene expression are described in Dataset S3.

In vitro cellular functions of M-MSCs, including cell viability, proliferation, self-renewal (colony forming unit-fibroblast; CFU-F), multipotency (differentiation capability into chondrogenic, osteogenic, or adipogenic lineages), *trans*-well migration, anti-inflammatory, and angiogenic assays, were evaluated as previously described [2,26,30]. Each cellular activity was quantified by digital image analysis using Image Pro 5.0 software (Media-Cybernetics, Rockville, MD, USA).

2.10. Statistical analysis

Data are reported as the mean ± standard error of the mean (SEM). Statistical significance was analyzed using GraphPad Prism 7.0 software (GraphPad Software, La Jolla, CA, USA) by either one-way or two-way ANOVA, followed by the Bonferroni *post-hoc* test. A p-value <0.05 was considered statistically significant.

3. Results

3.1. Two-photon IVM imaging for the transplanted M-MSCs and bladder vasculature

To directly visualize the dynamic interplay between the transplanted M-MSCs and bladder vasculature, we employed two-photon IVM. This method has several advantages for repeated and long-term imaging of living tissues due to efficient detection, increased imaging depth, minimal optical scattering, reduced unspecific excitation, and low phototoxicity and photobleaching in surrounding tissues [31]. Acute IC/BPS was induced in BALB/c-nu immune-compromised mice, first by hydrochloride (HCl) instillation and then by transplant of 1×10^5 M-MSCs stably harboring GFP directly into the outer layer of the anterior wall and dome of the bladder [19]. Three days after transplantation, the animals were anesthetized, the bladder was surgically exposed by making a small incision in the abdomen [19,20], and the bladder was examined by two-photon IVM toward outer layers of the bladder close to the M-MSC injection site (Fig. 1A). To outline the blood vessels, Texas red-conjugated Dextran was administrated by orbital injection at the time of imaging [25].

To minimize distress and movement throughout image acquisition, only a minimal incision was made, and the bladder was mounted between a cover glass stage and a custom-made organ plate (Fig. S1A). Histologic examination of bladder tissues showed that inflammatory responses were minimal, indicating minimal distress during the two-photon IVM procedures (Fig. S1B). Cells positive for GFP (GFP^+) were found by initially scanning through the bladder. A video-rate recording was performed, and then high-resolution z-stack images were acquired from the outer layers of bladder within an average 223.4 μm range

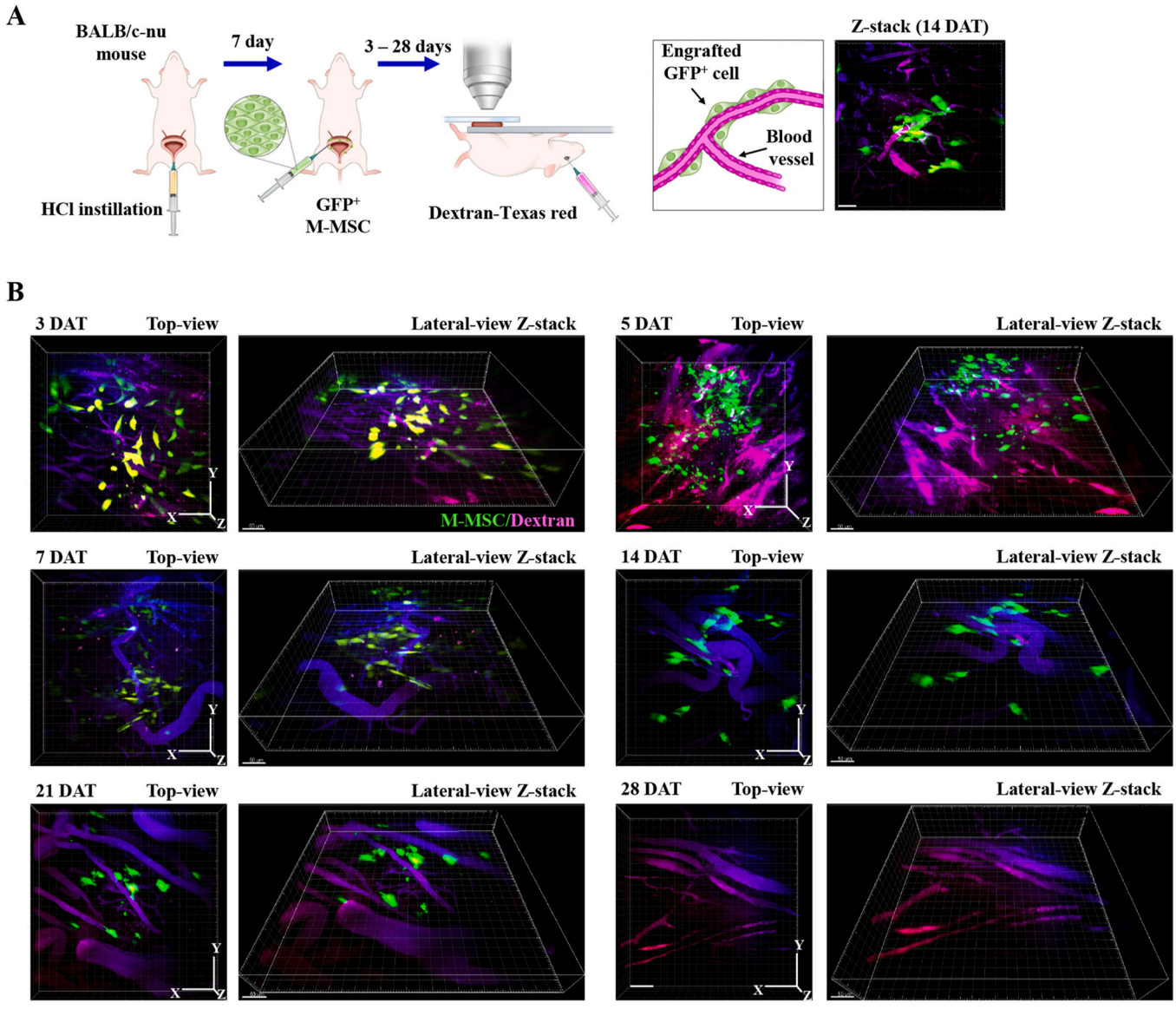

Fig. 1. Two-photon intravital microscopy of transplanted M-MSCs in living animals. **(A)** Experimental overview of two-photon intravital microscopy (IVM) of GFP^+ M-MSCs and bladder vasculature following transplantation into the bladder wall of IC/BPS mice. An example of a two-photon IVM image at 14 days after transplantation (DAT) is presented in the diagram. **(B)** Top (left) and lateral (right) projections of the z-stack images of two-photon IVM for longitudinal visualization of the bladder in a representative mouse (#1) from 3 to 28 DAT. The transplanted M-MSCs and bladder blood vessels are visualized by GFP (green) and Texas-red signals (purple-blue). Two-photon IVM results for two other mice (#2 and #3) are presented in Fig. S2. Video-rate imaging and z-stack 3D construction results of five independent mice (#1–5) over the whole experimental period are presented as Video S1–S5. The high-resolution z-stacks were imported into IMARIS for image processing and further quantitative analysis. Scale bar, 50 μm. (For interpretation of the references to colour in this figure legend, the reader is referred to the Web version of this article.)

(114–334 μm) (**Supplementary Videos**). After image acquisition, XYZ stacks were imported into IMARIS software for the creation of 3-dimensional (3D) representations (Figs. 1B and S2).

Our initial aim was to longitudinally visualize the distribution of the engrafted M-MSCs in live animals and to observe their dynamic interaction with the bladder vascular in same living animals over a period of weeks following transplantation. The two-photon IVM imaging revealed that the number of GFP$^+$ engrafted cells in host mice rapidly declined from 7 DAT; were sustained for a further 14 days; and then disappeared by 28 DAT ($n = 5$; Fig. 1B and Video S1−S5). The biological kinetics data was in line with a previous report that showed high apoptotic rates of engrafted M-MSCs at the early engraftment phase [20]. In this early period (3 and 5 DAT), multiple GFP$^+$ fields were identified throughout the bladder with a heterogenous distribution to the vasculature, based on a wide range of distance to bladder blood vessels (Figs. 1B and S2A). As the number of engrafted cells decreased from 7 DAT, the majority of

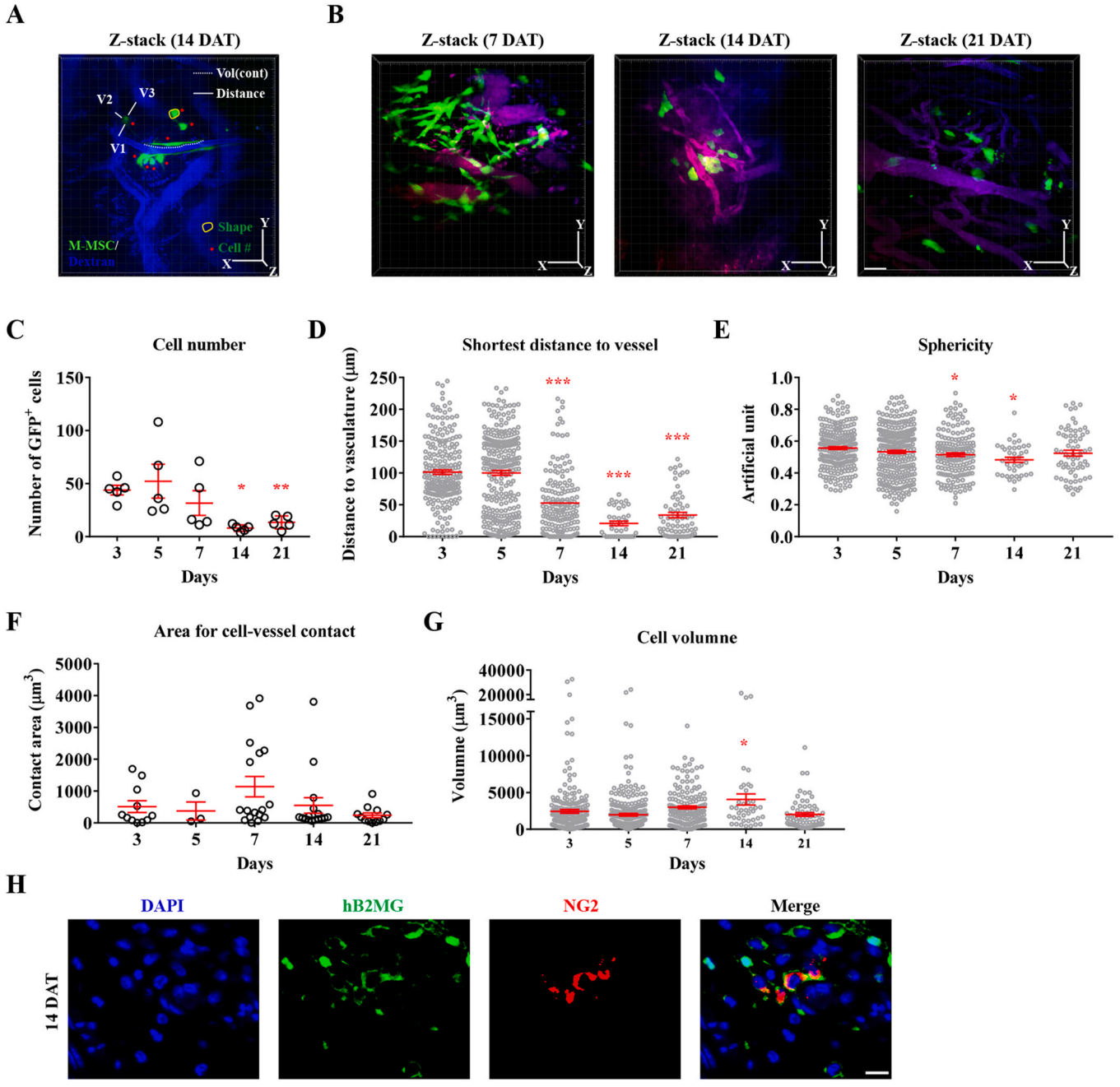

Fig. 2. Quantitative analysis for live two-photon IVM in the IC/BPS mice bladders. (A) Representative z-stack image at 14 DAT (mouse_#3) showing typical perivascular location including schematic overview for the quantification of cell number, volume, sphericity, distance to three proximal blood vessels, and their contact area. **(B)** Representative z-stack images acquired during two-photon IVM at 7, 14, and 21 DAT. Note that the engrafted GFP$^+$ cells were located in proximity to blood vessels at these time points. Scale bar, 50 μm. **(C—G)** Quantification results for number **(C)**, shortest distance to blood vessel **(D)**, sphericity (1.0, perfect sphere; 0, not spherical, **E**), contact area to vessel **(F)**, and cell volume **(G)** of the engrafted GFP$^+$ cells. Data from five independent mice are shown as dot plot of mean ± SEM. Statistical analyses were performed using one-way ANOVA with Bonferroni post-hoc tests. *$p < 0.05$, **$p < 0.01$, ***$p < 0.001$ relative to the 3 DAT group. Source data are available in Dataset S4. **(H)** Representative confocal micrographs (magnification, × 1000; scale bar, 10 μm) showing co-stain with human B2MG (hB2MG, green) and NG2, a pericyte marker (red), in the bladder sections of the HCl-IC nude mice at 14 DAT. Nuclei were counter-stained with DAPI (blue). (For interpretation of the references to colour in this figure legend, the reader is referred to the Web version of this article.)

the GFP$^+$ cells were mainly observed in proximity to blood vasculature for a supply of oxygen and nutrients. The perivascular localization of GFP$^+$ cells became clearly visible at 14 DAT, including a few GFP$^+$ cells that integrated along the blood vessels with pericyte-like morphology (Figs. 1A, B, and S2B). Although not all GFP$^+$ cells were engrafted at the surface of blood vessels at 21 DAT, they were localized close to the bladder vasculature and disappeared by 28 DAT.

Supplementary video related to this article can be found at https://doi.org/10.1016/j.biomaterials.2021.121277.

3.2. Quantitative analysis of intravital imaging for engraftment of M-MSCs into bladder

To quantitatively analyze the two-photon IVM imaging results, the

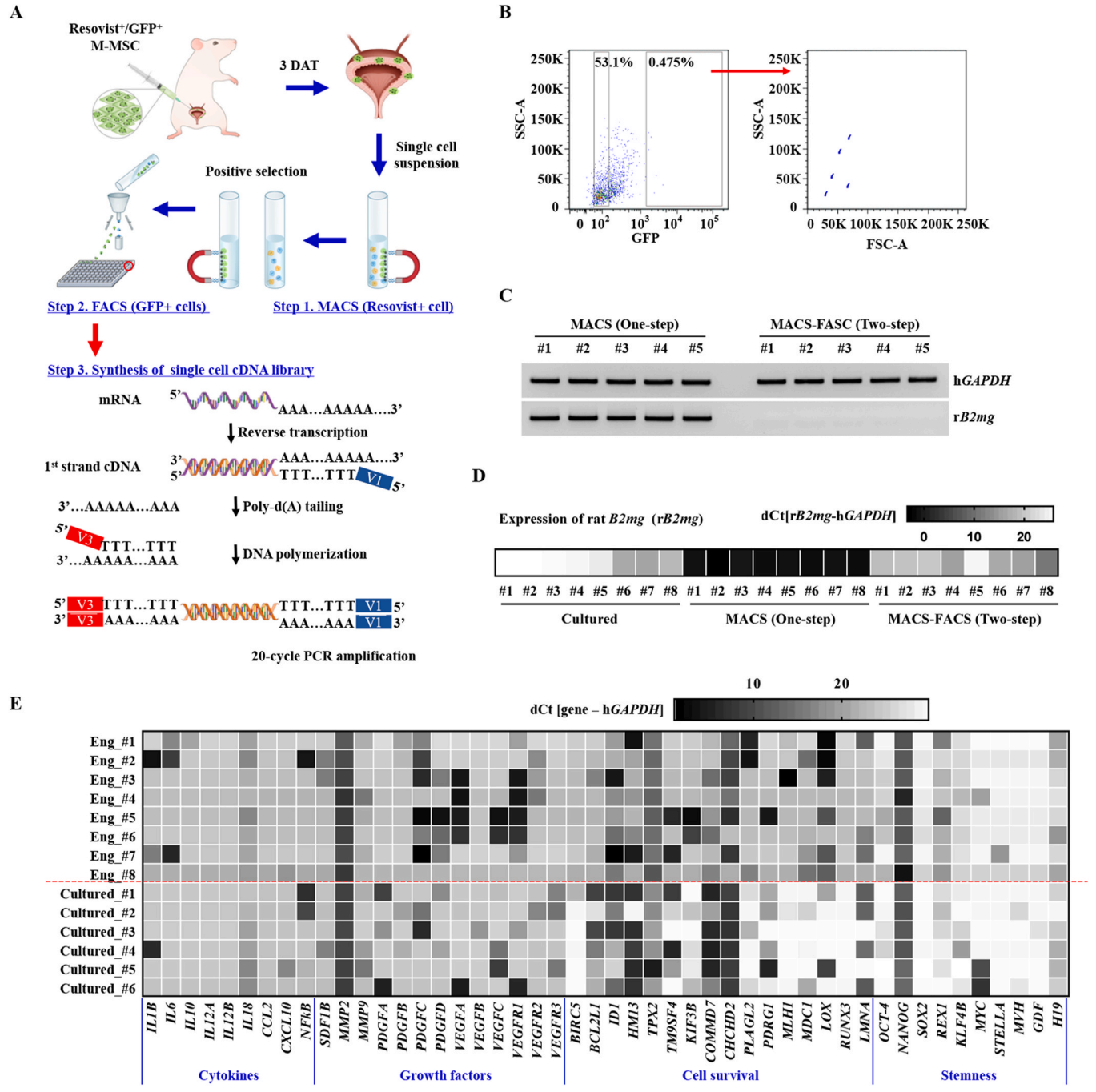

Fig. 3. Isolation and single cell transcriptome analysis of the engrafted M-MSCs. **(A)** Overview of single cell transcriptome analysis of the engrafted cells in rat IC/BPS bladder at 3 days after transcription (DAT) with Resovist$^+$/GFP$^+$ double-labeled M-MSCs, which were highly purified by consecutive MACS−FACS sorting. **(B)** FACS cytogram for isolation of GFP$^+$ cells from the MACS sorted Resovist$^+$ cells. The live Resovist$^+$/GFP$^+$ cells were gated by forward (FSC) and side (SSC) scatters. Double positive cells were then transferred individually into a single well of a 96-well plate for single cell cDNA library synthesis. **(C)** Representative results of gel electrophoresis showing expression of human *GAPDH* (*hGAPDH*) and rat *B2mg* (*rB2mg*) housekeeping genes from one-step MACS or two step MACS−FACS sorting procedures. **(D and E)** Heatmap analysis of Ct values from RQ-PCR experiments for the expression of the *rB2mg* **(D)** and human genes relating to the indicated biological process **(E)** using the indicated single cell cDNA libraries. Expression level is shown as delta Ct values relative to h*GAPDH* expression. The single cell libraries were synthesized from the cultured M-MSCs (Cultured_#1–6) and compared with MACS−FACS sorted engrafted cells (Eng_#1–8). Source data are available in Dataset S4.

number, volume, and sphericity of the engrafted GFP$^+$ cells were measured. In addition, the shortest distance between the GFP$^+$ cells and three proximal blood vessels was measured. Their contact area was measured when the engrafted cells were perivascularly located (Fig. 2A and B). GFP$^+$ engrafted cells were more abundant at 3 and 5 days (43.8 $\pm$ 10.03 and 52.2 $\pm$ 35.63, respectively, within approximate dimensions of 454 $\times$ 454 $\times$ average 50 μm^3) and were heterogeneously distributed in the bladder blood vessels (101.4 $\pm$ 53.29 and 100.1 $\pm$ 62.29 μm, respectively), in line with the two-photon IVM results (Fig. 2C and D, and Video S1−S5). Compared with the early engraftment phase, the distance between the engrafted cells and bladder vasculature became shorter from 7 DAT (52.87 $\pm$ 49.58 μm), and reduced by up to 20.72 μm on average by 14 DAT (Fig. 2D). As the engraftment site-to-vasculature distance ratio decreased from 7 DAT, the sphericity (with a perfectly round cell defined as 1) of GFP$^+$ cells decreased (Fig. 2E), and were observed to have a more spindle-like morphology (Fig. 2B). This perivascular localization concomitant with reduced sphericity indicated that the engrafted GFP$^+$ cells integrated along the blood vessels with pericyte-like morphology. Throughout the entire study, the engrafted GFP$^+$ cells had a similar contact area with the blood vessels, peaking at 7 DAT (Fig. 2F), and the volume of the engrafted cells was little changed, peaking at 14 DAT (Fig. 2G).

To further analyze the perivascular integration of the transplanted M-MSCs, the bladder tissues were immuno-stained with antibodies specific to human B2MG (hB2MG) to track the engrafted cells and then stained with antibody to NG2 proteoglycan, a pericyte specific marker. Consistent with the two-photon IVM results, the majority of the hB2MG$^+$ cells were perivascularly located and co-expressed NG2 at 14 DAT (Fig. 2H). Taken together, two-photon IVM imaging demonstrated that transplanted M-MSCs progressively contribute to perivascular cells and can be used to monitor the spectrum of *in vivo* M-MSC behavior in the bladder of living IC/BPS animals.

3.3. Single cell transcriptome of the engrafted M-MSCs in an acute animal model of IC/BPS

To understand the molecular signature of the engrafted M-MSCs in a pathological micro-environment, the engrafted cells were analyzed by genome-wide transcriptome profiling. Because MSCs typically have a poor *in vivo* engraftment efficacy, direct FACS of such low frequency engrafted cells was associated with increased assay times and decreases in yield and purity. To overcome these technical limitations, we implemented two consecutive sorting processes to improve the purity and homogeneity of the M-MSCs, consisting of MACS, followed by FACS. The resulting cells were then analyzed by single cell transcriptome analysis (Fig. 3A).

For positive MACS sorting, the GFP$^+$ M-MSCs were labeled with Resovist, a clinically approved superparamagnetic iron oxide [32,33]. Then, 1 $\times$ 10^6 Resovist-labeled GFP$^+$ M-MSCs were transplanted into the outer bladder layer of IC/BPS rats [19]. The Resovist labeling had a minimal effect on cell viability, and the magnetic beads were observed to be retained inside cells for 7 days of *in vitro* cell culture (Figs. S3A and B). When the engrafted cells were isolated by MACS−FACS sorting, a very low frequency of Resovist$^+$/GFP$^+$ double positivity was detected (approximately 0.475% of the initial number of MACS-sorted cells) (Fig. 3B). The double-purified cells were transferred individually into a single well of a 96-well plate using a ARIAIII cell sorter (Fig. 3A), and then single cell transcriptome libraries were synthesized following the T7-primed amplification procedure [27,28].

Single cell libraries were prepared from either the cultured M-MSCs (Cultured_#1–6) or the Resovist$^+$/GFP$^+$ engrafted cells (Eng_#1–8) that were isolated from the IC/BPS bladders at 3 DAT. These libraries were initially screened for the presence of contaminating host cells and showed little expression of rat-specific β2 microglobin (r*B2mg*) mRNA (Fig. 3C and D). The MACS-only sorted engrafted cells had a high proportion of contaminating host cells (Fig. S3C), unlike those sorted by a single FACS step (Figs. S3D and E).

Next, the synthesized single cell transcriptome libraries were characterized by examining the expression of genes related to stem cell engraftment, including i) cytokines, ii) chemokines, iii) matrix metalloprotease, iv) growth factors, v) cell survival, and vi) stemness. As shown in Fig. 3E, the engrafted cells showed up-regulated expression of interleukin-6 (*IL6*), platelet-derived growth factor subunit-C (*PDGFC*), *PDGFD*, vascular endothelial growth factor-A (*VEGFA)*, *VEGFR1*, and lysyl oxidase (*LOX*). Therefore, we applied single cell genome-wide profiling to freshly isolated double-positive, highly purified engrafted cells after transplantation.

3.4. Transcriptome properties of the engrafted cells in an acute animal model of IC/BPS

To elucidate the molecular mechanisms modulating the engraftment process, we compared the single cell transcriptome profiles of the engrafted and cultured M-MSCs. Both the principal component analysis (PCA) and scatter plot revealed that the engrafted cells in the IC/BPS bladders had a distinct molecular characteristic from the cultured cells before transplantation (Fig. 4A and B). According to the PCA result, the engrafted cells showed a high level of heterogeneity, compared with the cultured cells (Fig. 4A).

MetaCore pathway analysis indicated that the engrafted cells could be characterized by the expression of genes involved in extracellular matrix (ECM), cell adhesion, and cytoskeleton, as well as YAP/TAZ and EGFR signaling pathways and biological processes (Figs. 4C and S4A, and Dataset S1). Enrichment of cell adhesion, ECM, and cytoskeleton modulated pathways was also observed when the engrafted cells were divided into two sub-populations (sub1: Eng_#3, #5–7; sub2: Eng_#1, #2, and #4) (Figs. S4B and C), supporting the significance of these biological processes for M-MSC engraftment into the IC/BPS bladder. In line with these results, GSEA of the single cell transcriptome datasets revealed that the engrafted cells were enriched by sets of genes related to neural cell adhesion molecule-1 (NCAM-1) interaction (normalized enrichment score [NES] = 1.720), NCAM signaling (NES = 1.690), the WNT pathway (NES = 1.710), and lysine-specific histone demethylase-1a (LSD1) targets (NES = 1.730), compared with the cultured cells (Figs. 4D, S5A, B, and Dataset S2).

3.5. The engrafted M-MSCs highly express FOS and CDK1 proteins

To identify the driver genes that orchestrate the M-MSC engraftment process, we performed gene network (MetaCore) and leading-edge (GSEA) analyses. The MetaCore analysis revealed that the single cell transcriptomes from the engrafted cells were characteristically represented by WNT- and cyclin G-associated gene networks (Fig. 4E), as well as CREB1- and NFκB-associated networks (Fig. S4D). In particular, the GSEA leading-edge analysis revealed that *FOS* and genes encoding collagen Type IV α chain (*COL4A1*, *COL4A2*, and *COL4A5*) were significantly up-regulated in the engrafted cells (Figs. S5C and D). The perivascular localization observed by two-photon IVM suggested the need to perform GSEA analysis using genesets involved in pericytes. The engrafted cells were significantly enriched in the PDGF- and PECAM1-related pathways (Figs. 4F, S6A, and B). Of importance, *FOS* and AP-1 (a heterodimeric complex formed with FOS) were expressed in the engrafted M-MSCs and were key genes in the PDGF related pathways (Figs. 4F and S6C).

To validate these results, we performed RQ-PCR analysis of these single cell cDNA libraries. Accordingly, the engrafted cell libraries, compared with libraries from cultured cells, showed distinct expression of genes representing WNT-, CREB1-, and NFκB-signaling, as well as cell cycle, proliferation, migration, mitochondria, oxygen-containing, endoplasmic reticulum stress, and pericytes (Figs. 5A, E, and S7). Among them, *FOS* and *CDK1* were also identified in the GSEA and MetaCore analyses, representing pericyte- and cell cycle-related

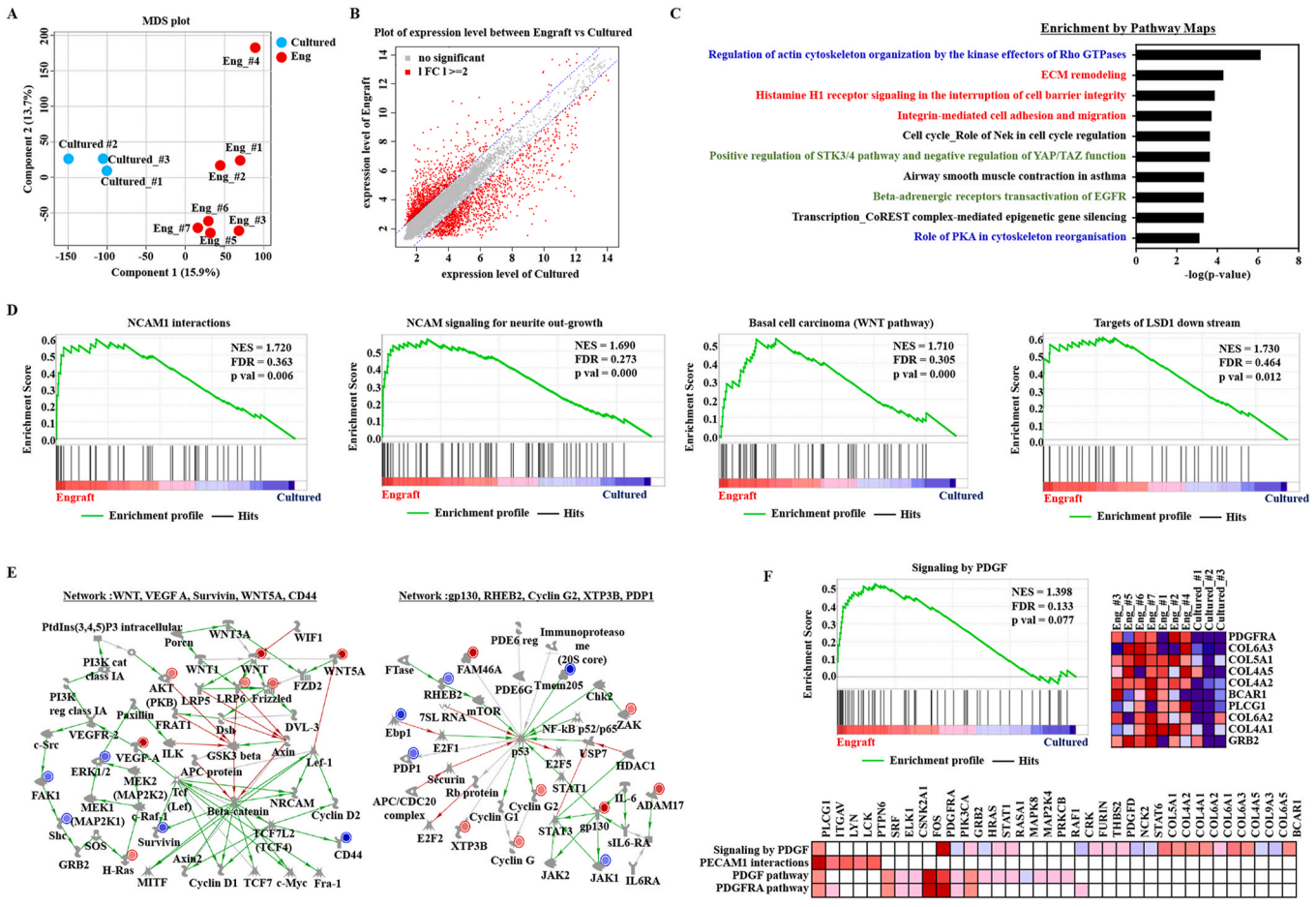

Fig. 4. Single cell transcriptome profiling characterizing the engrafted M-MSCs. **(A and B)** Principal component analysis (PCA, **A**) and scatter plot **(B)** comparing the three cultured (Cultured_#1–3) and seven engrafted (Eng_#1–7) single cell transcriptomes. **(C and D)** The 10 most highly enriched pathway maps by MetaCore analysis **(C)** and enrichment plots from geneset enrichment analysis (GSEA) **(D)** characterizing the engrafted cells. NES, normalized enrichment score; FDR, false discovery rate. **(E)** Representative enriched gene networks of the engrafted cells by MetaCore analysis. They are illustrated by overlaying the experimental value as fold-change in the engrafted versus cultured cells. Up- and down-regulated genes are indicated in red and blue, respectively. **(F)** Enrichment (left) and heatmap (right) plots of GSEA and leading-edge analysis (bottom) using genesets related to the pericyte biologcial process. (For interpretation of the references to colour in this figure legend, the reader is referred to the Web version of this article.)

processes, respectively. Furthermore, both genes were significantly up-regulated in the bladders of IC/BPS rats transplanted with M-MSCs (Fig. 5F). In line with these results, the hB2MG^{+} M-MSCs engrafted in the IC/BPS bladders showed high expression of FOS and CDK1 proteins, as determined by immunofluorescence staining analysis (Fig. 5G).

3.6. Roles of FOS and CDK1 in the migratory and anti-inflammatory functions of M-MSCs

To explore the biological significance of these findings, we expressed shRNA specific to *FOS* or *CDK1* (sh*FOS* or sh*CDK1*) in the M-MSCs (Figs. 6A and S8A) and examined their core functions, including self-renewal, migration, anti-inflammation, and pro-angiogenic capacities, which are responsible for the beneficial effects of MSC therapy [34]. Silencing of *FOS* or *CDK1* led to significant defects in chemoattraction to PDGF, indicative of impaired mobilization and engraftment (Fig. 6B). The knock-down (KD) of *FOS* or *CDK1* reduced the CFU-F activity, which represents clonogenic activity (Figs. 6C and S8B). However, these KDs had little effect on multi-potency, based on chondrogenic, osteogenic, and adipogenic differentiation of KD-M-MSCs (Fig. S8C) compared with M-MSCs harboring control empty shRNA (shEmpty). The MSCs expressing sh*CDK1* showed a decrease in proliferation rate, which was observed after 5 days of *FOS* silencing (Fig. 6D). Importantly, the conditioned medium (CM) from M-MSCs harboring sh*FOS* or sh*CDK1* had reduced anti-inflammatory activity, based on significant inhibition of the secretion of tumor necrosis factor (TNF)-α, IL-6, and CCL-2/MCP1 pro-inflammatory proteins by the lipopolysaccharide (LPS)-stimulated macrophages (Figs. 6E, F, and S8D). The reduced anti-inflammatory capacity by silencing of *FOS* or *CDK1* was further validated based on the increased expression levels of cytokines including *Tnf-α*, *Il-6*, *Il-18*, *Ccl-2*, and *Ccl-7* in the LPS-stimulated macrophages (Figs. 6G and S8D). The angiogenic potency was minimally affected by the CM from *FOS* or *CDK1* silenced MSCs in the Matrigel tube formation assay (Fig. S8E). Taken together, these *in vitro* functional assays demonstrate that *FOS* and *CDK1* play an important role, particularly in the migratory and anti-inflammatory capacities of MSCs, which are crucial factors for treating IC/BPS.

3.7. In vivo significance of FOS and CDK1 on M-MSC therapy for IC-BPS

To examine whether defects in the migratory and anti-inflammatory functions caused by *FOS* or *CDK1* silencing could affect the therapeutic potency of M-MSCs, we injected 1×10^6 M-MSCs harboring sh*FOS* or sh*CDK1* directly into the bladders of rats with HCl-induced IC/BPS and compared the outcome with control cells harboring the empty shRNA. To precisely investigate functional outcomes, we performed awake filling cystometry, which allows long-term evaluation of bladder voiding function in free-moving animals [19,20]. IC/BPS is a syndrome

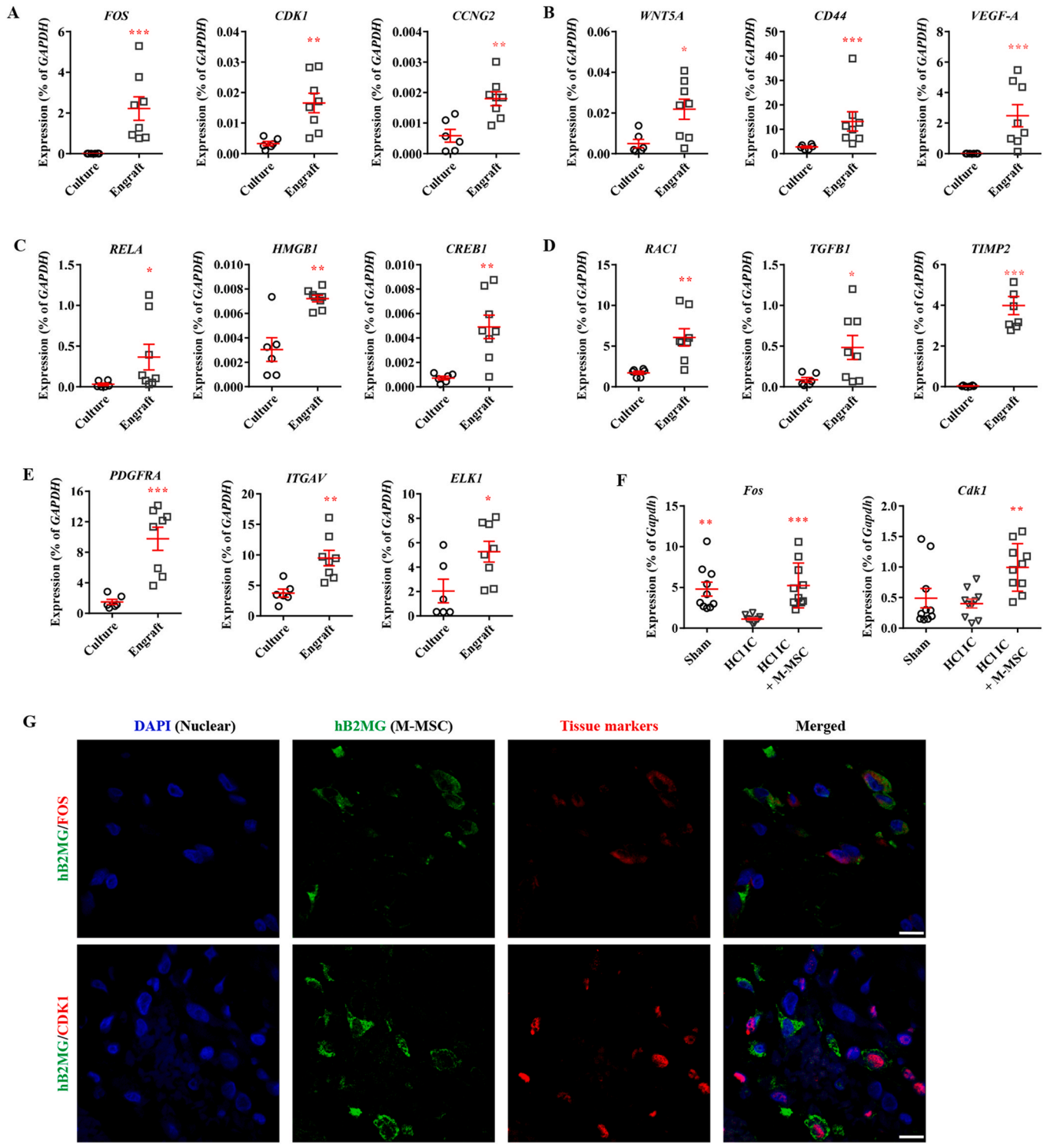

Fig. 5. Up-regulation of *FOS* and *CDK1* in the engrafted M-MSCs. **(A–E)** RQ-PCR analysis of signficant genes representing cell cycle- **(A)**, WNT- **(B)**, and NFκB- **(C)** signaling, and cell migration- **(D)** and pericyte- **(E)** related pathways, as determined by analysis of the single cell cDNA libraries from the engrafted (Engraft, $n = 8$) and cultured (Culture, $n = 6$) cells. Expression is presented as % relative to h*GAPDH* expression. **(F)** RQ-PCR analysis of rat *Fos* and *Cdk1* in the indicated bladder tissues in the HCl-induced IC/BPS (HCl-IC) animal model at 1 week after tranplantation of 1×10^6 M-MSCs. Expression is presented as % relative to rat *Gapdh* expression ($n = 10$). The quantitative results are shown as dot plot of mean ± SEM (*p < 0.05, **p < 0.01, ***p < 0.001 compared with the culture **(A—E)** or HCl-IC **(F)** groups according to the Bonferroni post-hoc test). **(G)** Representative confocal micrographs (magnification, × 1000; scale bar, 10 μm) of human B2MG (hB2MG, green) co-stained with either FOS or CDK1 (red) in the bladder sections of the HCl-IC rats transplanted with GFP^+ M-MSCs. Nuclei were counter-stained with DAPI (blue). (For interpretation of the references to colour in this figure legend, the reader is referred to the Web version of this article.)

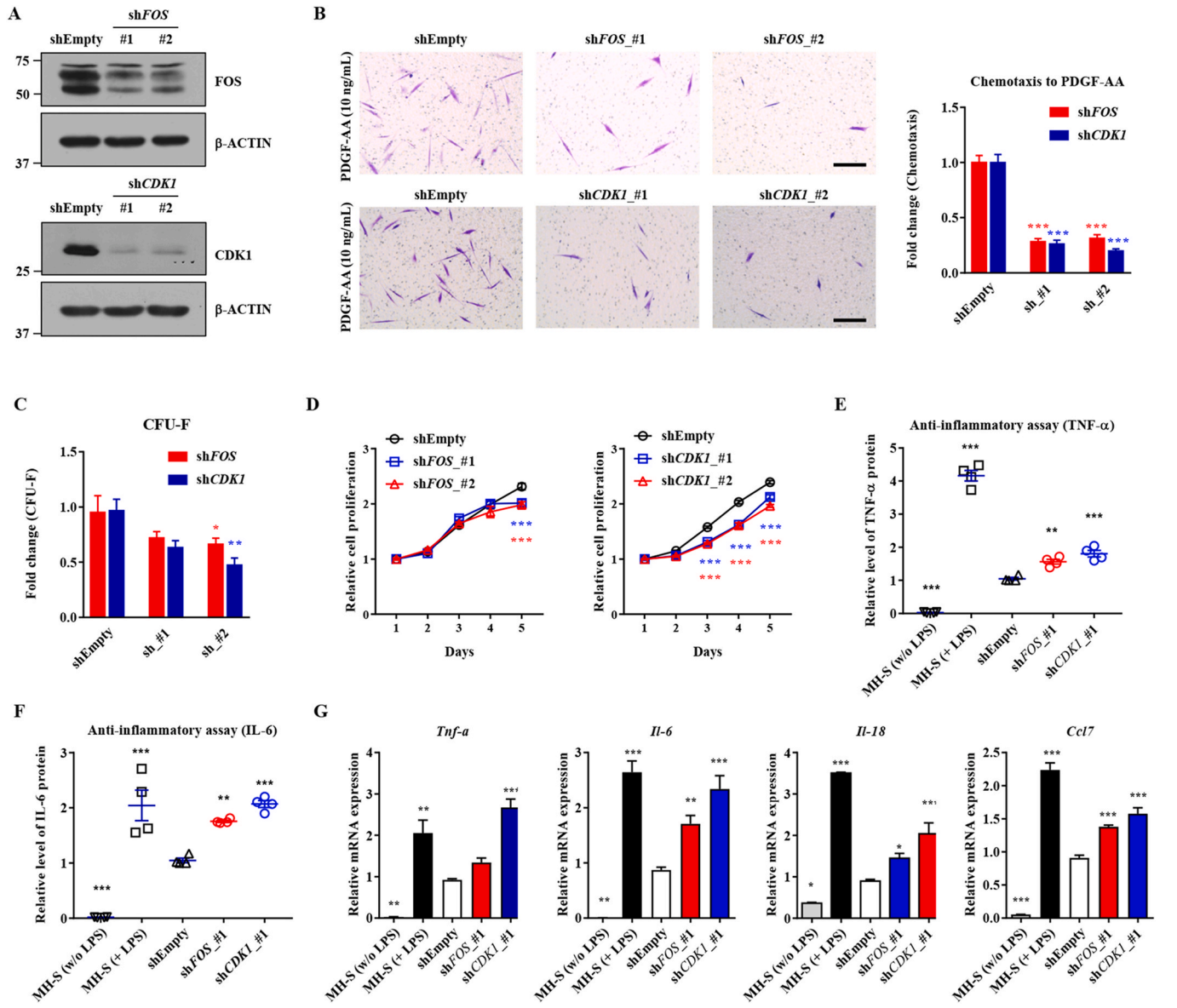

Fig. 6. Critical roles of *FOS* and *CDK1* in the core functions of M-MSCs. **(A)** Western blot analysis of the M-MSCs at 4 days after infection with lentivirus containing shRNA for *FOS* or *CDK1* (sh*FOS* or sh*CDK1*). β-ACTIN was used as a loading control. **(B)** Representative images (magnification, × 200; scale bar, 100 μm; left) and quantitative data ($n = 7$; right) showing chemotactic activity of M-MSCs harboring sh*FOS* or sh*CDK1* toward 10 ng/mL PDGF-AA. **(C and D)** CFU-F **(C)** and proliferation **(D)** assays in the *FOS* or *CDK1* silenced M-MSCs. For the CFU-F assay, 60 cells were seeded in 6-well culture plates and cultured for 14 days, and then the number of colonies was quantified. **(E–G)** Anti-inflammatory assays using conditioned medium (CM) were prepared using the indicated cells. The secretion of TNF-α **(E)** and IL-6 **(F)** protein from MH-S, a murine alveolar macrophage cell line stimulated with LPS for 8 h, were quantified by ELISA assay, and the expression of the indicated pro-inflammatory cytokines **(G)** was quantified by RQ-PCR assay. All quantification results are represented as ratios relative to empty control (shEmpty) and presented as means ± SEM ($n = 4$). Statistical analyses were performed using one-way **(E–F)** or two-way **(B–D)** ANOVA with Bonferroni *post-hoc* tests. *$p < 0.05$, **$p < 0.01$, ***$p < 0.001$ relative to shEmpty group.

characterized by urinary urgency, frequency, pelvic pain, and nocturia [8]. As previously reported [19], irregular voiding patterns were observed in the HCl-IC group, with characteristic reduction in the micturition interval (MI; 31.34 ± 13.65 vs. 109.1 ± 21.36 s; $p < 0.001$), micturition volume (MV; 0.16 ± 0.09 vs. 0.66 ± 0.12 mL; $p < 0.001$), micturition pressure (MP; 36.29 ± 25.5 vs. 63.32 ± 19.47 cmH_2O; $p < 0.001$), bladder capacity (BC; 0.21 ± 0.09 vs. 0.73 ± 0.14 mL; $p < 0.001$), and residual volume (RV; 0.04 ± 0.04 vs. 0.07 ± 0.05 mL; $p < 0.05$), compared with sham-operated rats (Fig. 7A and B).

A single transplantation of M-MSCs with empty shRNA into rats with IC/BPS significantly improved these voiding parameters (Fig. 7A and B). The M-MSC therapy significantly ameliorated the frequency of contraction during the non-voiding period (non-voiding contraction; NVC), which is the most common factor for evaluating bladder voiding function in clinical care. Importantly, these beneficial outcomes were hardly observed in the IC/BPS rats with transplantation of M-MSCs expressing sh*FOS* or sh*CDK1* (Fig. 7A and B). Consistent with the results from awake cystometry, administration of the *FOS* or *CDK1* silenced M-MSCs failed to restore histological damage that was typically observed in the bladders of IC/BPS patients, including severe urothelial denudation, mast cell infiltration, fibrosis, and apoptotic cell death (Figs. 7C and S9).

Patients with IC/BPS experience a vague pelvic pain that is aggravated by bladder filling. M-MSC therapy has been reported to ameliorate visceral organ crosstalk, as well as the severity and frequency of abdominal pain or discomfort in IC/BPS [19]. To determine whether

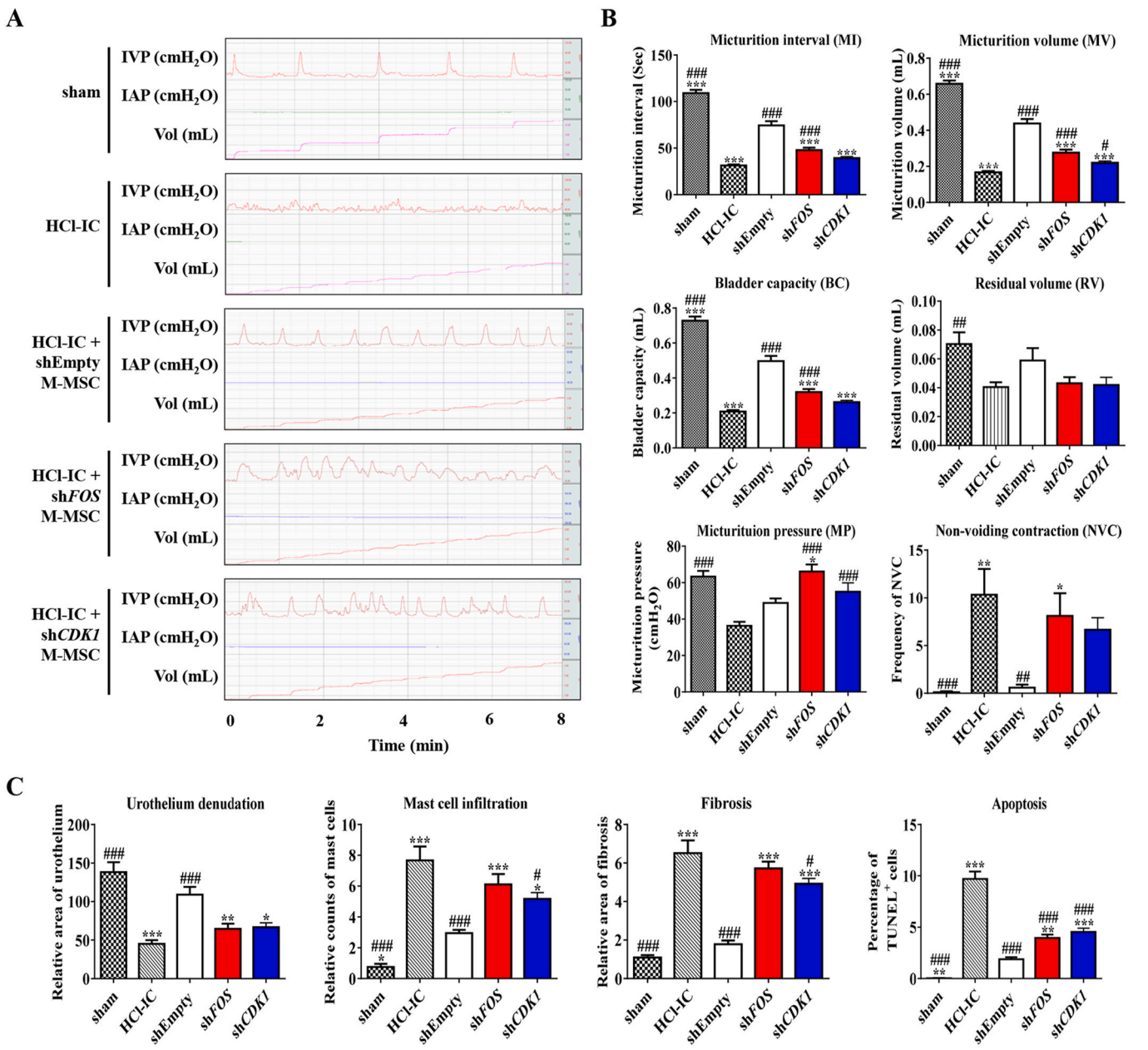

Fig. 7. FOS and CDK1 determined therapeutic potency of M-MSCs in HCl-IC rats. **(A)** Representative awake cystometry results and **(B)** quantitative bladder voiding parameters 1 week after the injection of 1×10^6 M-MSCs expressing sh*FOS*, sh*CDK1*, or shEmpty constructs. Quantitative results from ten independent animals in each group are presented as the mean ± SEM. Sham: sham-operated. **(C)** Quantification of histological examniations for urothelium denudation (hematoxylin and eosin (H&E) staining), mast cell infiltration (Toluidine blue staining), fibrosis (Masson's trichrome staining), and apoptosis (TUNEL staining) in the indicated bladder tissues. Data were normalized to the sham group and presented as the mean ± SEM ($n \geq 18$). *p < 0.05, **p < 0.01, ***p < 0.001 compared with the shEmpty group; #p < 0.05, ##p < 0.001, ###p < 0.001 compared with the HCl-IC group with Bonferroni post-test. (For interpretation of the references to colour in this figure legend, the reader is referred to the Web version of this article.)

FOS and CDK1 could affect the beneficial effects of M-MSC therapy in controlling the pain and visceral hypersensitivity of IC/BPS, we measured pain score in animals with HCl-induced IC/BPS and examined the anatomical interactions between mast cells and nerve fibers, as well as the expression of genes associated with visceral hypersensitivity, such as nerve growth factor (Ngf), Tnf-α and tachykinin receptor-1(Tacr1) [35]. Measurement of tactile allodynia in rat paws using the von Frey hairs up-down method [36] showed that M-MSCs significantly ameliorated the threshold of paw withdrawal response, which was reduced in rats with HCl instillation. However, the silencing of *FOS* and *CDK1* abolished the relief of pain provided by M-MSCs (Fig. S10A). Consistent with these findings, M-MSCs harboring *FOS* or *CDK1* shRNA failed to restore the anatomical interactions between mast cells and nerve fibers in the IC/BPS bladder, which were significantly reduced by M-MSC therapy (Figs. S10B and C). The *FOS* or *CDK1* silenced M-MSCs had little effect on the amelioration of induction of *Ngf*, *Tnf*-α, and *Tacr1* (Fig. S10D). Collectively, these results demonstrate the crucial roles of FOS and CDK1 in the therapeutic potency of M-MSCs for treating IC/BPS regarding not only pathology with bladder functional alteration but also with pain.

3.8. Defective engraftment of FOS and CDK1 silenced M-MSCs in the IC/BPS animals

We next examined whether *FOS* and *CDK1* could critically affect the engraftment of M-MSCs in the IC/BPS bladders. The immunofluorescence staining revealed that the hB2MG $^{+}$ engrafted cells were less abundant in the bladders administrated with *FOS* or *CDK1* silenced M-MSCs, compared with shEmpty control cells (Figs. 8A, B and S11).

To compare the *in vivo* engraftment capacity of these cells in live animals, we employed M-MSCs stably expressing Nano-lantern, a chimera of enhanced Renilla luciferase and Venus fluorescent protein with high efficiency of bioluminescence resonance energy transfer [24], and compared the bioluminescence intensities of the transplanted cells by optical imaging. Consistent with the results of hB2MG immunofluorescence staining, the IC/BPS immune-compromised mice transplanted with M-MSCs harboring sh*FOS* and sh*CDK1* showed significantly reduced bioluminescence activity than those with shEmpty cells throughout the whole experimental period (Figs. 8C, D and S12). Taken together, these results demonstrate that *FOS* and *CDK1* are key modulators for the engraftment of M-MSCs into the IC/BPS bladders, and can determine the therapeutic potency of these cells.

4. Discussion

The precise mode of action of MSC therapies has not been fully resolved, which is critical for rationalizing their use and developing strategies to enhance treatment efficacy. The present study describes the advanced approaches to characterize *in vivo* behaviors of the engrafted MSCs in pathological environments, by employing two-photon IVM imaging and single cell transcriptome analysis of purified cells. Accordingly, we demonstrate that *FOS* and *CDK1* play a key role in modulating the engraftment and anti-inflammatory capacities of M-MSCs for treating IC/BPS *in vivo*.

IC/BPS is a chronic inflammatory condition that affects the submucosal and muscular layers of the bladder and disrupts the integrity of the urothelium. Unfortunately, its etiology is not fully understood, and few

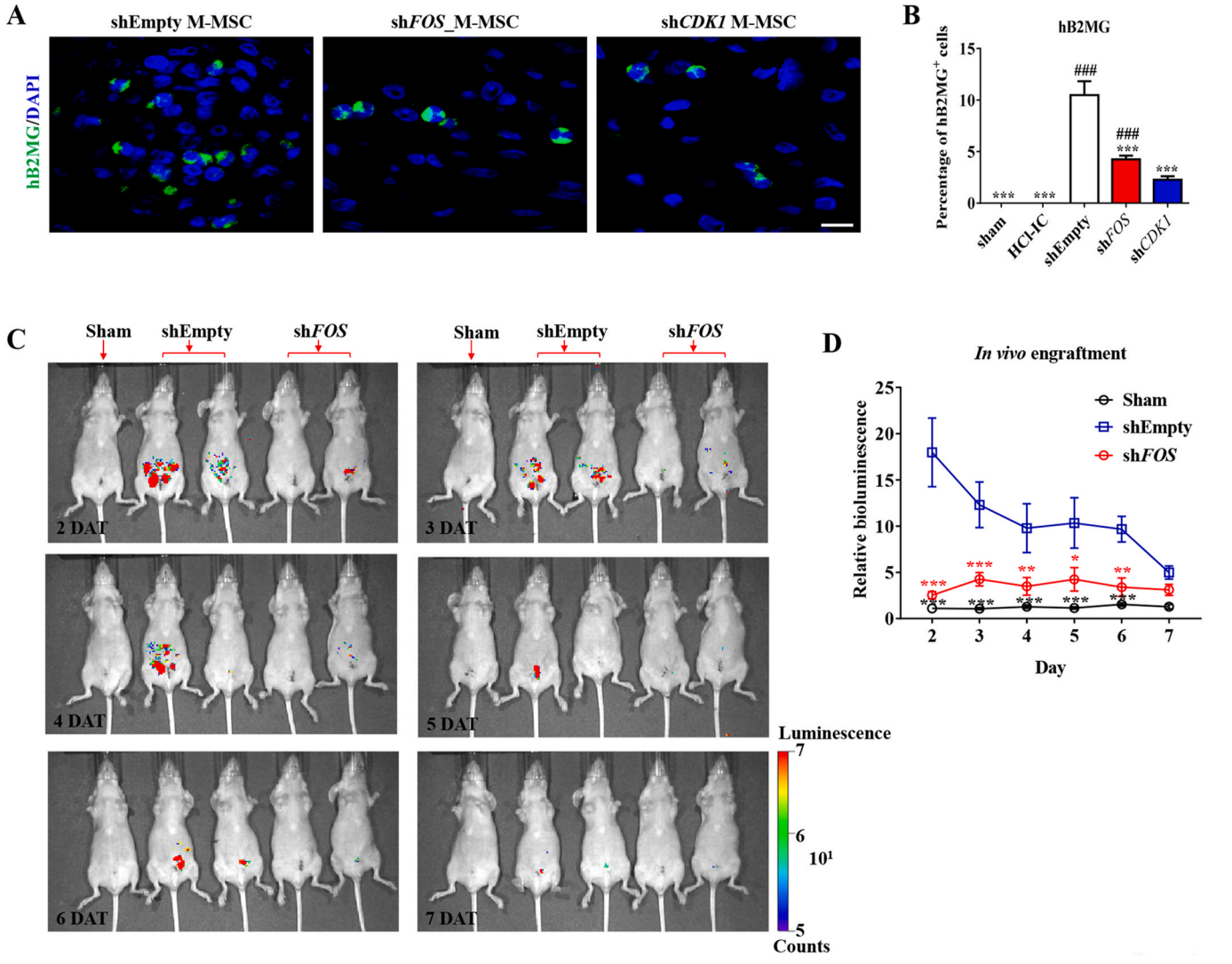

Fig. 8. Impaired *in vivo* engraftment of the *FOS* or *CDK1* silenced M-MSCs. **(A and B)** Representative confocal micrographs (magnification, × 1000; scale bar, 10 μm, **A**) and quantification results ($n = 20$, **B**) for the engrafted GFP^{+} M-MSCs expressing human B2MG (hB2MG, green) in the bladder tissue sections of HCl-IC animals. Nuclei were counter-stained with DAPI (blue). **(C and D)** Imaging of biolouminescence activies from the M-MSCs expressing sh*FOS* or shEmpty contructs at the indicated day after transplantation (DAT) in the HCl-IC animals. **(C)** The representative images were obtained at 15 min after intraperitonieal injection of 150 μg/mL coelenterazine (200 μL), a substrate of Renilla luciferase. **(D)** Quantification results for bioluminescence signals are presented as means ± SEM ($n = 6$). Statistical significance was examined by one-way **(B)** or two-way **(D)** ANOVA with Bonferroni *post-hoc* tests. *p < 0.05, **p < 0.01, ***p < 0.001 compared with the shEmpty group; ###p < 0.001 compared with the HCl-IC group with Bonferroni *post-hoc* test. (For interpretation of the references to colour in this figure legend, the reader is referred to the Web version of this article.)

effective treatments have been developed. MSC therapy is a promising strategy to regenerate damaged urothelial cells and to establish an anti-inflammatory or immunomodulatory micro-environment. Indeed, we demonstrated the promise of MSC transplantation as a therapeutic option for treating this intractable disorder in rat models representing the different pathological conditions [19,20,23]. However, the bio-distribution and cellular properties of engrafted cells in pathological environments have not been properly analyzed *in vivo*, hampering our understanding of mechanisms underlying functional improvement after transplantation of MSCs.

Current understanding of MSC migration and engraftment processes has been mainly derived from histological analysis of engrafted cells in target organs. Although these methods provide spatial information, they can only provide static insights at discrete time-intervals in different mice. Therefore, intravital imaging is a very attractive method to longitudinally observe the dynamic *in vivo* behavior and bio-distribution of MSCs while engrafting into the pathological environments. Two-photon IVM allows deep high-resolution visualization and has advantages over traditional confocal microscopy methods, such as reduced autofluorescence and photobleaching effects, increased imaging depth, and minimal photodamage to surrounding brain tissue [31]. Using this method, the present study sought to develop an *in vivo* imaging model that enables analysis of the entire spectrum of engrafted MSC behavior at single cell resolution.

Besides two-photon IVM, we chose to use MSCs derived from hESCs instead of adult tissues. The PSC-derived cells have greater therapeutic benefits than adult tissue-derived MSCs in a wide range of animal disease models. Indeed, we recently reported the improved therapeutic efficacy and long-term engraftment capacity of M-MSCs in an acute IC/BPS animal model identical to that used in this study [19] and in a chronic model induced by LPS instillation [20]. The long-term engraftment capacity of M-MSCs may benefit longitudinal *in vivo* imaging of key characteristics associated with engraftment in a single animal for up to 1 month. Therefore, this intravital imaging approach could be tested with adult tissue derived MSCs in a further study.

The two-photon IVM imaging revealed the pericyte-like nature and progressive perivascular localization of the engrafted M-MSCs that peaked at 14 DAT, which was further supported by immunofluorescence staining and single cell transcriptome analysis. Although the *in vivo* behaviors of the engrafted cells were visualized within the same animal, we did not longitudinally track the individual engrafted cell over the entire course of engraftment. To visualize the cellular dynamics over days or weeks, imaging chambers or windows are required to record repetitive images at the same location [37]. Therefore, the development of a specialized bladder imaging chamber is warranted to advance the preliminary visualization of the engrafted MSCs and perivascular niche presented here to aid quantification of biological dynamics, kinetics, and cell-niche interactions.

Due to severe inflammatory, ischemic, and apoptotic micro-environments in the injured tissues, MSCs rarely engraft and replace damaged cells after *in vivo* administration [38]. The poor engraftment efficiency of M-MSCs indicates that the source/number of cells was too low to assess their molecular profile, particularly at the genome-wide level. Based on FACS results, the percentage of engrafted M-MSCs was approximately 0.343% of cells in a whole bladder at 3 DAT, and 0.053% at 5 DAT. In the present study, the combination of FACS and MACS sorting was shown to rapidly isolate the rare engrafted M-MSCs and to minimize host cell contamination, allowing transcriptomic analysis at a single cell level. Accordingly, the single cell analysis indicated that the engrafted cells were highly represented by several biological pathways and processes related to cell adhesion, ECM, and cytoskeleton functions. In line with two-photon IVM results, the engrafted M-MSCs up-regulated genes related to pericyte signaling pathways in which *FOS* plays a critical role. In addition, WNT-, CREB1-, and NFκB-signaling pathways were differentially expressed in the engrafted cells, compared with *in vitro* cultured counterparts.

Among them, the WNT signaling cascade pathway has previously been considered as a potential key mechanism for elucidating the therapeutic effects of M-MSCs in preclinical studies for IC/BPS [19,20,23]. Considering that this growth factor promotes regeneration of the epithelium [39], the up-regulation of WNT genes in the engrafted M-MSCs may protect the urothelial layer of the bladder against further environmental damage and in parallel establish a micro-environment favorable for tissue repair. This notion is well-correlated with the recent findings that genetically modified stem cells over-expressing WNT5A or WNT10A improved functional bladder regeneration [40,41]. Similarly, WNT5A promotes the differentiation of MSCs into type II alveolar epithelial cells through noncanonical WNT signaling [42]. In line with these results, the silencing of *WNT5A* in M-MSCs significantly reduced the *in vitro* chemotatic response to PDGF and clonogenic CFU-F activity, indicating impaired migration and self-renewal potency (Fig. S13). Additional studies are needed to evaluate the *in vivo* effects of WNT5A, particularly on the engraftment process of MSCs in a pathological micro-environment.

Recently, we demonstrated that glutathione (GSH), an abundant cellular thiol and major determinant of the redox equilibrium, is essential to maintain the stemness and migration capacities of MSCs, determining their therapeutic efficiency in asthma [26,43] and graft-versus-host disease (GVHD) [2,34]. Mechanistically, CREB1 activated nuclear factor erythroid-2 related factor 2, a well-known master regulator of redox homeostasis that orchestrates GSH dynamics in MSCs, enforcing their core functions [2]. Moreover, the CREB1 pathway is important for the naïve pluripotency of murine ESCs and the primitive state of human MSCs by induction of ascorbic acid 2-glucoside, a stable vitamin-C derivative [44]. In line with these findings, forskolin, a CREB1 activator, induces the naïve state of human ESCs [45,46] and stimulates somatic cell reprogramming [47]. Therefore, CREB1 plays multiple roles, not only by enforcing the engraftment capacity of MSCs in the pathological conditions, but also by preserving the naïve or primitive states of stem cells, which are preserved in specific *in vivo* niches. These naïve or primitive states are extremely difficult to stabilize *in vitro*, largely due to the accumulation of epigenetic abnormalities [22] and oxidative stress provoked by supra-physiological stimulation [26].

According to our single transcriptomic analysis, the *FOS* and *CDK1*-associated genes were differentially expressed in the engrafted cells and validated by *in vitro* functional assays and *in vivo* assessment of M-MSCs to treat IC/BPS. FOS, a stress-response transcription factor, promotes the production of COX2-mediated PGE2, promoting the cytoprotective effect of MSCs under various stress conditions [48]. In addition, FOS functions as a direct target of ATF6 to protect premature cellular aging of human MSCs, characterized by loss of endomembrane homeostasis [49]. Therefore, up-regulation of FOS in the engrafted MSCs in the IC/BPS bladder could be beneficial, not only by preserving their core functions, but also by promoting adaptation into new cellular and inflammatory micro-environments.

CDK1 is a protein kinase that controls the transition from the G2 phase to the M phase of the cell cycle. Mitotic protein kinases, such as CDK1, aurora kinases, and polo-like kinase-1 (PLK1), are critical for maintaining several functions of stem cells [29,30,50]. In our previous report, MSCs over-expressing *PLK1* enhanced their migratory and immunomodulatory activities, resulting in their superior therapeutic efficacy in a humanized mouse model of GVHD [30]. In addition, CDK1 stimulated the migration and invasion activities of bladder cancer cells in addition to proliferation and cell cycle progression. However, it should be noted that bladder cancer patients with high expression of CDK1 have been associated with unfavorable clinical characteristics, including high tumor grade, lymphovascular and muscularis propria invasion, and distant metastasis [29]. In addition, FOS promotes the reprogramming of BM-MSCs into chondroblastic osteocarcoma [51]. Although minimal tumorigenic potency of M-MSCs derived from hESCs was reported [4,19,21], safety concerns regarding the engrafted M-MSCs with high expression of CDK1 or FOS should be thoroughly

investigated in a future study.

5. Conclusion

MSCs are being investigated for the treatment of diverse diseases, and show promising outcomes from animal models and clinical trials [8, 52–54]. To facilitate the translation of preclinical studies into clinical practice, the precise *in vivo* behaviors of the engrafted cells after transplantation should be analyzed regarding their biological properties. This study provides an optimized strategy to characterize the distributions, properties, and intercellular interactions of engrafted cells *in vivo*. This approach should be utilized in IC/BPS models subjected to other types of pathological insults or with other intractable bladder voiding dysfunction disorders, such as overactive bladder and detrusor underactivity [8]. Finally, this study provides a better understanding of the mechanisms and safety concerning stem cell therapy, and the need to optimize transplantation protocols prior to clinical trials.

Author contributions

H.W.Y. and S.L. contributed equally to this work. Conceptualization: D.M.S. and M.S.C.; Methodology: D.M.S., H.W.Y., S.L., and J.K.K.; Investigation: H.W.Y., S.L., H.J., Y.K., J.H.S., H.Y., C.M.R., J.H., J.L., S. S., and S.L.; Writing – Original Draft: D.M.S., H.W.Y., and S.L.; Writing – Review & Editing: D.M.S., M.S.C., H.W.Y., and S.L.; Funding Acquisition: D.M.S., M.S.C., S.L., and J.K.K.; Resources: K.S.H., and H.M.C.; Data Curation: D.M.S., M.S.C., H.W.Y., S.L., and H.J.; Supervision: D.M. S., M.S.C., and J.K.K.

Data availability

The transcriptome data discussed in this study have been deposited into the NCBI Gene Expression Omnibus and are accessible through GEO Series accession number GSE162982.

Declaration of competing interest

The authors declare that they have no known competing financial interests or personal relationships that could have appeared to influence the work reported in this paper.

Acknowledgements

We thank Dr. Eunjoo Song for technical support with the two-photon IVM analysis. This research was supported by a grant from the Korean Health Technology R&D Project, Ministry of Health & Welfare, Republic of Korea (HI18C2391), by the Basic Science Research Program through the National Research Foundation of Korea (NRF-2021R1A2C2005790, 2021R1I1A1A01043792, and NRF-2020R1A2C1007789); a NRF MRC grant funded by the Korean government (MSIP) (NRF-2018R1A5A2020732); and a grant (2019IP0868 and 2021IP0019) from the Asan Institute for Life Sciences, Asan Medical Center, Seoul, Korea.

Appendix A. Supplementary data

Supplementary data to this article can be found online at https://doi.org/10.1016/j.biomaterials.2021.121277.

References

[1] J. Zonderland, L. Moroni, Steering cell behavior through mechanobiology in 3D: a regenerative medicine perspective, Biomaterials 268 (2021) 120572.
[2] J. Lim, J. Heo, H. Ju, J.-W. Shin, Y. Kim, S. Lee, et al., Glutathione dynamics determine the therapeutic efficacy of mesenchymal stem cells for graft-versus-host disease via CREB1-NRF2 pathway, Science Advances 6 (2020) eaba1334.
[3] I. Martin, J. Galipeau, C. Kessler, K. Le Blanc, F. Dazzi, Challenges for mesenchymal stromal cell therapies, Sci. Transl. Med. 11 (2019).
[4] K.S. Hong, D. Bae, Y. Choi, S.W. Kang, S.H. Moon, H.T. Lee, et al., A porous membrane-mediated isolation of mesenchymal stem cells from human embryonic stem cells, Tissue Eng. C Methods 21 (2015) 322–329.
[5] B.H. Cha, J.S. Kim, A. Bello, G.H. Lee, D.H. Kim, B.J. Kim, et al., Efficient isolation and enrichment of mesenchymal stem cells from human embryonic stem cells by utilizing the interaction between integrin alpha5beta1 and fibronectin, Adv. Sci. (Weinheim, Baden-Wurttemberg, Germany) 7 (2020) 2001365.
[6] R. Goetzke, J. Franzen, A. Ostrowska, M. Vogt, A. Blaeser, G. Klein, et al., Does soft really matter? Differentiation of induced pluripotent stem cells into mesenchymal stromal cells is not influenced by soft hydrogels, Biomaterials 156 (2018) 147–158.
[7] D. Sheyn, S. Ben-David, G. Shapiro, S. De Mel, M. Bez, L. Ornelas, et al., Human induced pluripotent stem cells differentiate into functional mesenchymal stem cells and repair bone defects, Stem Cells Transl Med 5 (2016) 1447–1460.
[8] J.H. Shin, C.M. Ryu, H.Y. Yu, D.M. Shin, M.S. Choo, Current and future directions of stem cell therapy for bladder dysfunction, Stem Cell Rev Rep 16 (2020) 82–93.
[9] Y. Shi, Y. Wang, Q. Li, K. Liu, J. Hou, C. Shao, et al., Immunoregulatory mechanisms of mesenchymal stem and stromal cells in inflammatory diseases, Nat. Rev. Nephrol. 14 (2018) 493–507.
[10] S.-G. Ong, B.C. Huber, W. Hee Lee, K. Kodo, A.D. Ebert, Y. Ma, et al., Microfluidic single-cell analysis of transplanted human induced pluripotent stem cell–derived cardiomyocytes after acute myocardial infarction, Circulation 132 (2015) 762–771.
[11] S. Kim, L. Lin, G.A.J. Brown, K. Hosaka, E.W. Scott, Extended time-lapse in vivo imaging of tibia bone marrow to visualize dynamic hematopoietic stem cell engraftment, Leukemia 31 (2017) 1582–1592.
[12] Y. Yuan, Z. Zhang, W. Hou, W. Qin, Z. Meng, C. Wu, In vivo dynamic cell tracking with long-wavelength excitable and near-infrared fluorescent polymer dots, Biomaterials 254 (2020) 120139.
[13] W. Li, R. Chen, J. Lv, H. Wang, Y. Liu, Y. Peng, et al., In vivo photoacoustic imaging of brain injury and rehabilitation by high-efficient near-infrared dye labeled mesenchymal stem cells with enhanced brain barrier permeability, Adv. Sci. (Weinheim, Baden-Wurttemberg, Germany) 5 (2018) 1700277.
[14] K.P. Kubelick, E.J. Snider, C.R. Ethier, S. Emelianov, Development of a stem cell tracking platform for ophthalmic applications using ultrasound and photoacoustic imaging, Theranostics 9 (2019) 3812–3824.
[15] M.N. McCracken, E.H. Gschweng, E. Nair-Gill, J. McLaughlin, A.R. Cooper, M. Riedinger, et al., Long-term in vivo monitoring of mouse and human hematopoietic stem cell engraftment with a human positron emission tomography reporter gene, Proc. Natl. Acad. Sci. U. S. A. 110 (2013) 1857–1862.
[16] C. Yang, X. Ni, D. Mao, C. Ren, J. Liu, Y. Gao, et al., Seeing the fate and mechanism of stem cells in treatment of ionizing radiation-induced injury using highly near-infrared emissive AIE dots, Biomaterials 188 (2019) 107–117.
[17] S. Upadhaya, O. Krichevsky, I. Akhmetzyanova, C.M. Sawai, D.R. Fooksman, B. Reizis, Intravital imaging reveals motility of adult hematopoietic stem cells in the bone marrow niche, Cell Stem Cell 27 (2020) 336–345, e334.
[18] C. Christodoulou, J.A. Spencer, S.A. Yeh, R. Turcotte, K.D. Kokkaliaris, R. Panero, et al., Live-animal imaging of native haematopoietic stem and progenitor cells, Nature 578 (2020) 278–283.
[19] A. Kim, H.Y. Yu, J. Lim, C.M. Ryu, Y.H. Kim, J. Heo, et al., Improved efficacy and in vivo cellular properties of human embryonic stem cell derivative in a preclinical model of bladder pain syndrome, Sci. Rep. 7 (2017) 8872.
[20] C.M. Ryu, H.Y. Yu, H.Y. Lee, J.H. Shin, S. Lee, H. Ju, et al., Longitudinal intravital imaging of transplanted mesenchymal stem cells elucidates their functional integration and therapeutic potency in an animal model of interstitial cystitis/bladder pain syndrome, Theranostics 8 (2018) 5610–5624.
[21] S.W. Lee, C.M. Ryu, J.H. Shin, D. Choi, A. Kim, H.Y. Yu, et al., The therapeutic effect of human embryonic stem cell-derived multipotent mesenchymal stem cells on chemical-induced cystitis in rats, Int. Neurourol. J. 22 (2018) S34–S45.
[22] J. Heo, J. Lim, S. Lee, J. Jeong, H. Kang, Y. Kim, et al., Sirt1 regulates DNA methylation and differentiation potential of embryonic stem cells by antagonizing Dnmt3l, Cell Rep. 18 (2017) 1930–1945.
[23] M. Song, J. Lim, H.Y. Yu, J. Park, J.Y. Chun, J. Jeong, et al., Mesenchymal stem cell therapy alleviates interstitial cystitis by activating wnt signaling pathway, Stem Cell. Dev. 24 (2015) 1648–1657.
[24] K. Saito, Y.F. Chang, K. Horikawa, N. Hatsugai, Y. Higuchi, M. Hashida, et al., Luminescent proteins for high-speed single-cell and whole-body imaging, Nat. Commun. 3 (2012) 1262.
[25] A. Masedunskas, R. Weigert, Intravital two-photon microscopy for studying the uptake and trafficking of fluorescently conjugated molecules in live rodents, Traffic 9 (2008) 1801–1810.
[26] E.M. Jeong, J.H. Yoon, J. Lim, J.W. Shin, A.Y. Cho, J. Heo, et al., Real-time monitoring of glutathione in living cells reveals that high glutathione levels are required to maintain stem cell function, Stem Cell Rep. 10 (2018) 600–614.
[27] K. Kurimoto, Y. Yabuta, Y. Ohinata, M. Saitou, Global single-cell cDNA amplification to provide a template for representative high-density oligonucleotide microarray analysis, Nat. Protoc. 2 (2007) 739–752.
[28] D.M. Shin, R. Liu, W. Wu, S.J. Waigel, W. Zacharias, M.Z. Ratajczak, et al., Global gene expression analysis of very small embryonic-like stem cells reveals that the Ezh2-dependent bivalent domain mechanism contributes to their pluripotent state, Stem Cell. Dev. 21 (2012) 1639–1652.
[29] J. Heo, B.J. Noh, S. Lee, H.Y. Lee, Y. Kim, J. Lim, et al., Phosphorylation of TFCP2L1 by CDK1 is required for stem cell pluripotency and bladder carcinogenesis, EMBO Mol. Med. 12 (2020), e10880.
[30] Y. Kim, H.J. Jin, J. Heo, H. Ju, H.Y. Lee, S. Kim, et al., Small hypoxia-primed mesenchymal stem cells attenuate graft-versus-host disease, Leukemia 32 (2018) 2672–2684.

[31] C. Scheele, C. Maynard, J. van Rheenen, Intravital insights into heterogeneity, metastasis, and therapy responses, Trends in cancer 2 (2016) 205–216.
[32] M.A. Kolecka, S. Arnhold, M. Schmidt, C. Reich, M. Kramer, K. Failing, et al., Behaviour of adipose-derived canine mesenchymal stem cells after superparamagnetic iron oxide nanoparticles labelling for magnetic resonance imaging, BMC Vet. Res. 13 (2017) 62.
[33] A.S. Arbab, E.K. Jordan, L.B. Wilson, G.T. Yocum, B.K. Lewis, J.A. Frank, In vivo trafficking and targeted delivery of magnetically labeled stem cells, Hum. Gene Ther. 15 (2004) 351–360.
[34] J. Lim, J. Heo, H.Y. Yu, H. Yun, S. Lee, H. Ju, et al., Small-sized mesenchymal stem cells with high glutathione dynamics show improved therapeutic potency in graft-versus-host disease, Clin. Transl. Med. 11 (2021) e476.
[35] A.P. Malykhina, C. Qin, B. Greenwood-van Meerveld, R.D. Foreman, F. Lupu, H. I. Akbarali, Hyperexcitability of convergent colon and bladder dorsal root ganglion neurons after colonic inflammation: mechanism for pelvic organ cross-talk, Neuro Gastroenterol. Motil. 18 (2006) 936–948.
[36] S.R. Chaplan, F.W. Bach, J.W. Pogrel, J.M. Chung, T.L. Yaksh, Quantitative assessment of tactile allodynia in the rat paw, J. Neurosci. Methods 53 (1994) 55–63.
[37] D. Fukumura, D.G. Duda, L.L. Munn, R.K. Jain, Tumor microvasculature and microenvironment: novel insights through intravital imaging in pre-clinical models, Microcirculation 17 (2010) 206–225.
[38] G.E. Salazar-Noratto, G. Luo, C. Denoeud, M. Padrona, A. Moya, M. Bensidhoum, et al., Understanding and leveraging cell metabolism to enhance mesenchymal stem cell transplantation survival in tissue engineering and regenerative medicine applications, Stem Cell. 38 (2020) 22–33.
[39] K. Shin, J. Lee, N. Guo, J. Kim, A. Lim, L. Qu, et al., Hedgehog/Wnt feedback supports regenerative proliferation of epithelial stem cells in bladder, Nature 472 (2011) 110–114.
[40] A.K. Sharma, M.I. Bury, N.J. Fuller, A.J. Marks, D.M. Kollhoff, M.V. Rao, et al., Cotransplantation with specific populations of spina bifida bone marrow stem/progenitor cells enhances urinary bladder regeneration, Proc. Natl. Acad. Sci. U. S. A. 110 (2013) 4003–4008.
[41] D.C. Snow-Lisy, E.C. Diaz, M.I. Bury, N.J. Fuller, J.H. Hannick, N. Ahmad, et al., The role of genetically modified mesenchymal stem cells in urinary bladder regeneration, PLoS One 10 (2015), e0138643.
[42] A. Liu, S. Chen, S. Cai, L. Dong, L. Liu, Y. Yang, et al., Wnt5a through noncanonical Wnt/JNK or Wnt/PKC signaling contributes to the differentiation of mesenchymal stem cells into type II alveolar epithelial cells in vitro, PLoS One 9 (2014), e90229.
[43] E.M. Jeong, J.W. Shin, J. Lim, J.H. Kim, H. Kang, Y. Yin, et al., Monitoring glutathione dynamics and heterogeneity in living stem cells, Int. J. Stem Cells 12 (2019) 367–379.
[44] S. Lee, J. Lim, J.H. Lee, H. Ju, J. Heo, Y. Kim, et al., Ascorbic acid 2-glucoside stably promotes the primitiveness of embryonic and mesenchymal stem cells through ten-eleven translocation- and cAMP-responsive element-binding protein-1-dependent mechanisms, Antioxidants Redox Signal. 32 (2020) 35–59.
[45] G. Duggal, S. Warrier, S. Ghimire, D. Broekaert, M. Van der Jeught, S. Lierman, et al., Alternative routes to induce naive pluripotency in human embryonic stem cells, Stem Cell. 33 (2015) 2686–2698.
[46] J. Hanna, A.W. Cheng, K. Saha, J. Kim, C.J. Lengner, F. Soldner, et al., Human embryonic stem cells with biological and epigenetic characteristics similar to those of mouse ESCs, Proc. Natl. Acad. Sci. Unit. States Am. 107 (2010) 9222–9227.
[47] J.S. Kim, Y.J. Hong, H.W. Choi, S. Choi, J.T. Do, Protein kinase A signaling is inhibitory for reprogramming into pluripotent stem cells, Stem Cell. Dev. 25 (2016) 378–385.
[48] N. Komatsu, M. Kajiya, S. Morimoto, S. Motoike, H. Yoshii, T. Iwata, et al., Cox2-mediated PGE2 production via p38/JNK-c-fos signaling inhibits cell apoptosis in 3D floating culture clumps of mesenchymal stem cell/extracellular matrix complexes, Biochem. Biophys. Res. Commun. (2020).
[49] S. Wang, B. Hu, Z. Ding, Y. Dang, J. Wu, D. Li, et al., ATF6 safeguards organelle homeostasis and cellular aging in human mesenchymal stem cells, Cell discovery 4 (2018) 2.
[50] J. Shin, T.W. Kim, H. Kim, H.J. Kim, M.Y. Suh, S. Lee, et al., Aurkb/PP1-mediated resetting of Oct4 during the cell cycle determines the identity of embryonic stem cells, Elife 5 (2016), e10877.
[51] Y. He, W. Zhu, M.H. Shin, J. Gary, C. Liu, W. Dubois, et al., cFOS-SOX9 Axis reprograms bone marrow-derived mesenchymal stem cells into chondroblastic osteosarcoma, Stem Cell Rep. 8 (2017) 1630–1644.
[52] A. Kim, D.-M. Shin, M.-S. Choo, Stem cell therapy for interstitial cystitis/bladder pain syndrome, Curr. Urol. Rep. 17 (2015) 1–9.
[53] C. Zhang, S.V. Murphy, A. Atala, Regenerative medicine in urology, Semin. Pediatr. Surg. 23 (2014) 106–111.
[54] H. Sadri-Ardekani, A. Atala, Regenerative medicine for the treatment of reproductive system disorders: current and potential options, Adv. Drug Deliv. Rev. 82–83 (2015) 145–152.